NGA-West2 Equations for Predicting Vertical-Component PGA, PGV, and 5%-Damped PSA from Shallow Crustal Earthquakes

Jonathan P. Stewart,[a)] M.EERI, **David M. Boore,[b)] Emel Seyhan,[c)]** M.EERI, and **Gail M. Atkinson,[d)]** M.EERI

We present ground motion prediction equations (GMPEs) for computing natural log means and standard deviations of vertical-component intensity measures (IMs) for shallow crustal earthquakes in active tectonic regions. The equations were derived from a global database with **M** 3.0–7.9 events. The functions are similar to those for our horizontal GMPEs. We derive equations for the primary **M**- and distance-dependence of peak acceleration, peak velocity, and 5%-damped pseudo-spectral accelerations at oscillator periods between 0.01–10 s. We observe pronounced **M**-dependent geometric spreading and region-dependent anelastic attenuation for high-frequency IMs. We do not observe significant region-dependence in site amplification. Aleatory uncertainty is found to decrease with increasing magnitude; within-event variability is independent of distance. Compared to our horizontal-component GMPEs, attenuation rates are broadly comparable (somewhat slower geometric spreading, faster apparent anelastic attenuation), V_{S30}-scaling is reduced, nonlinear site response is much weaker, within-event variability is comparable, and between-event variability is greater. [DOI: 10.1193/072114EQS116M]

INTRODUCTION

Prediction equations for the horizontal component of ground motions have received considerably more attention than those for the vertical. Nonetheless, there is an engineering need to predict vertical ground motions for certain structures (e.g., long span bridges, nuclear power plants, dams), and as a result the Pacific Earthquake Engineering Research (PEER) Center organized a program to develop ground motion prediction equations (GMPEs) for the vertical-component of ground motions as part of the NGA-West2 project (Bozorgnia et al. 2014).

Previous work on characterization of vertical motions has either focused on vertical-to-horizontal ratios (V/H ratios; e.g., Ambraseys and Douglas 2003, Bozorgnia and Campbell 2004, Bommer et al. 2011, Gülerce and Abrahamson 2011, Akkar et al. 2014) or has developed vertical GMPEs for particular geographic regions (Ambraseys et al. 2005, Bindi et al.

[a)] University of California, Los Angeles, CA, email: jstewart@seas.ucla.edu
[b)] U.S. Geological Survey, MS 977, 345 Middlefield Rd., Menlo Park, CA 94025
[c)] Risk Management Solutions, 7575 Gateway Blvd., Newark, CA, 94560
[d)] University of Western Ontario, London, Ontario, Canada

2011) or for global application (Campbell and Bozorgnia 2003). V/H ratios are typically used to modify a horizontal response spectrum (uniform hazard spectrum or scenario spectrum) to produce a corresponding vertical spectrum. The principal limitation of V/H ratios is that the vertical-component may scale differently from the horizontal with respect to moment magnitude (**M**), source-site distance, and site condition. While such differences can in principle be captured by V/H models conditioned on these explanatory variables, there are some practical difficulties—for example, differences in distance attenuation trends may be associated with multiple model components, including fictitious depth terms, geometric spreading terms, anelastic attenuation terms, and nonlinear site response terms. It is difficult to capture all of these effects in a V/H formulation where the vertical prediction is linked to the horizontal GMPE. Another difficulty is that the standard deviation terms may be different.

Accordingly, we take the approach of developing a vertical GMPE directly, without the use of a reference horizontal model. Our work expands upon previous vertical GMPEs by using a large global data set for active crustal regions, over a broad period range, overcoming problems with previous vertical GMPEs pointed out by Bommer et al. (2011; i.e., lack of consistent databases for horizontal and vertical components; models not applicable for **M** > 7 events due to small database size; lack of consideration of oscillator periods <0.1 s; use of hypocentral distance as the distance metric; lack of uncertainty characterization).

We utilize a similar database and function as for the analysis for the horizontal-component GMPEs described by Boore et al. (2014; hereafter, BSSA14). Although we used a similar form for the equations providing the mean in natural log units (hereafter referred to as the mean, with the use of natural log being implied), most of the coefficients have changed, as has the function describing the aleatory uncertainty model. Subsequent sections of this paper provide a complete set of equations for the model, describe the process by which the model coefficients were obtained, and show the ground motion trends revealed by the vertical-component GMPEs. We conclude with a summary and statement of limitations. We note that the model described in this manuscript is substantially modified relative to an earlier vertical GMPE presented in a report chapter by Stewart et al. (2013; hereafter, SSBA13). Our model coefficients are provided in Table A1 of the online Appendix.

DATA SET USED FOR MODEL DEVELOPMENT

DATA SOURCE AND SELECTION CRITERIA

We use an NGA-West2 flatfile that contains site and source information, along with distance parameters and computed ground motion intensity measures (IMs; Ancheta et al. 2014). The version of the flatfile that we used in our analysis is dated 29 August 2013 and contains 21,539 vertical-component ground motions. Our data selection is largely the same as for the horizontal-component GMPEs as described by BSSA14.

Some particularly important aspects of the common data selection criteria with BSSA14 are requiring availability of magnitude, distance, and site metadata, using only data from active crustal regions, excluding records from large structures, and screening of data at large distance as a function of magnitude and instrument type (Figure 1 of BSSA14). We consider ground motions from Class 1 (CL1: main shocks) and Class 2 (CL2: aftershocks)
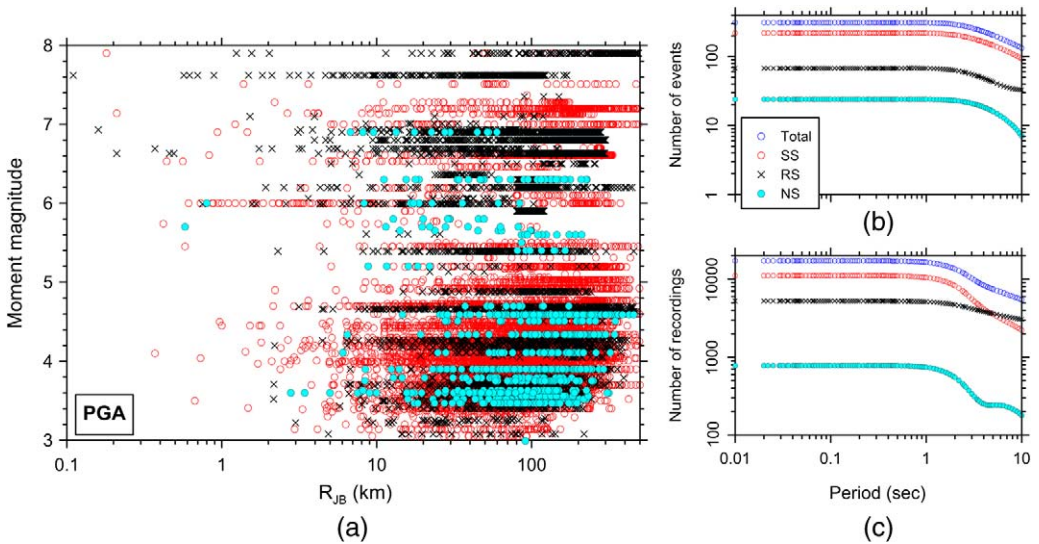
Figure 1. (a) Distribution of data by fault type used to develop the vertical GMPEs: SS = strike-slip, NS = normal-slip, RS = reverse-slip. (b) Number of events and (c) number of recordings vs. period.

events, using the minimum centroid R_{JB} separation of 10 km from Wooddell and Abrahamson (2014) based on subjective interpretation of results from exploratory analysis. Records are screened to include only those periods within the usable frequency band for the vertical-component, and to exclude any records flagged as questionable by manual inspection (as described by Ancheta et al. 2014; specifically, we require that the "Spectra Quality Flag" under Column JK in the flatfile equals 0). There are some differences in the actual records used for the vertical- versus the horizontal-component GMPEs because of the differences in the usable frequency band and the spectra quality flag.

Application of these criteria results in 17,089 recordings for peak ground acceleration (PGA), although only a subset of these records is used for developing the base-case GMPEs, as described further below.

INTENSITY MEASURES AND PREDICTOR VARIABLES

The ground motion IMs comprising the dependent variables of the GMPEs include vertical-component PGA, peak ground velocity (PGV), and 5%-damped pseudo-spectral acceleration (PSA). We do not include equations for peak ground displacement (PGD), which we believe to be too sensitive to the low-cut filters used in the data processing to be a stable measure of ground shaking.

The main predictor variables used in our regression analyses are moment magnitude **M**, R_{JB} distance (closest distance to the surface projection of the fault plane), site parameter V_{S30}, and fault type. Fault type represents the classification of events as strike slip (SS), normal slip (NS), or reverse slip (RS), based on the plunge of the *P*- and *T*-axes (see Table 2.2 in

Boore et al. 2013). Almost the same fault type assignments would be obtained using rake angle, with SS events being defined as events with rake angles within 30 degrees of horizontal, and RS and NS being defined for positive and negative rake angles not within 30 degrees of horizontal, respectively. We did not consider hanging wall effects, as our use of the R_{JB} distance measure implicitly accounts for larger motions over the hanging wall for fault dip angles in the range of 25 to 70 degrees, which are well represented in the NGA-West2 data (Ancheta et al. 2014). Each of the predictor variables was taken from the NGA-West2 database flatfile.

DATA DISTRIBUTIONS

Figure 1a shows the **M** and R_{JB} distribution of data used to develop our GMPEs. As with the horizontal-component, the magnitude range is widest for strike-slip (SS) and reverse-slip (RS) earthquakes and narrowest for normal-slip (NS). Figure 1b–c show the numbers of recordings and earthquakes used in equation development, differentiated by fault type. There is a decrease in available data for periods longer than several seconds, although the fall off is less rapid than for the horizontal-component (Figure 2 of BSSA14). In the parts of metadata space where the data are relatively sparse, the GMPEs are less well resolved (i.e., close distances, long periods, **M**-scaling for NS events).
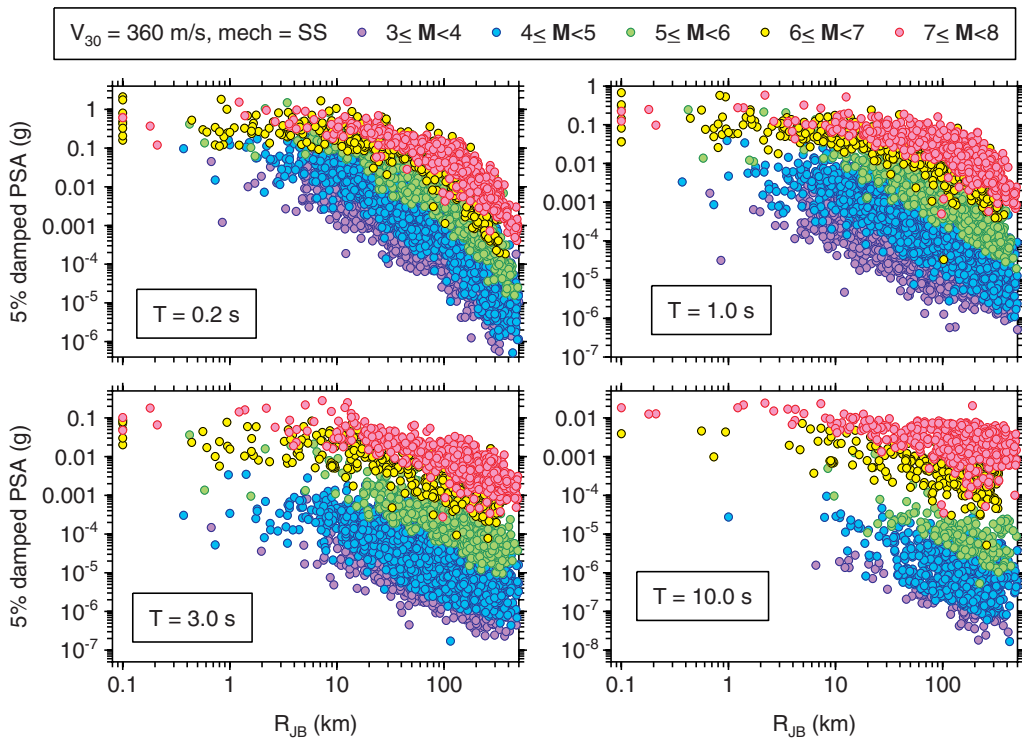

Figure 2. *PSA* at four periods for strike-slip earthquakes. All amplitudes adjusted to $V_{S30} = 360$ m/s using the soil amplification factors of this study.

The data distribution with respect to the time-averaged velocity in the upper 30 m (V_{S30}) is practically identical to that for the horizontal-component. As shown in Figure 4 of BSSA14, most of the records are for sites with $V_{S30} = 200–800$ m/s, but there is a sufficient number of records on relatively hard rock ($V_{S30} > 800$ m/s) to constrain the stiff portions of the site-amplification functions. The V_{S30} data include measured and inferred velocities (Seyhan et al. 2014).

Figure 2 shows nonparametric plots of vertical *PSA* at four periods for strike slip events. The data have been adjusted to $V_{S30} = 360$ m/s, using the SSBA13 site amplification function with some modification, as described in the *Development and Interpretation of Model Coefficients* section below. These plots reveal features we sought to accommodate in our GMPEs: **M**-dependent geometric spreading; anelastic attenuation effects evident from curvature in the decay of log ground motions versus log distance for distances beyond about 80 km; and strongly nonlinear (and period dependent) magnitude dependence of amplitude scaling at a fixed distance.

THE GROUND MOTION PREDICTION EQUATIONS

The function for the vertical-component GMPEs presented in this paper is similar to that used in BSSA14, having components for source- (or event) scaling, path-scaling, site-scaling, and aleatory variability. The selected function is:

$$\ln Y = F_E(\mathbf{M}, mech) + F_P(R_{JB}, \mathbf{M}) + F_S(V_{S30}, \mathbf{M}, mech, R_{JB}) + \varepsilon_n \sigma(\mathbf{M}) \qquad (1)$$

where $\ln Y$ represents the natural logarithm of a vertical ground motion intensity measure (PGA and PGV; 5%-damped PSA); F_E, F_P, and F_S represent period-dependent functions for source (event), path, and site effects, respectively; ε_n is the fractional number of standard deviations of a single predicted value of $\ln Y$ away from the mean (e.g., $\varepsilon_n = -1.5$ is 1.5 standard deviations smaller than the mean); and σ is the total standard deviation of the model. The predictor variables are $\mathbf{M}$, *mech*, R_{JB}, and V_{S30}. Parameter $mech = 0$, 1, 2, and 3 for unspecified, SS, NS, and RS, respectively. The units of PGA and PSA are g and PGV is cm/s. The main difference between BSSA14 equations and the vertical-component equations is that for the vertical-component equations we found no need for a sediment depth term, and our analysis showed that σ is a function only of $\mathbf{M}$ (and not R_{JB} and V_{S30}).

ELEMENTS OF LN MEAN MODEL (SOURCE, PATH, AND SITE FUNCTIONS)

The source (event) function is given by:

$$F_E(\mathbf{M}, mech) = \begin{cases} e_0 U + e_1 SS + e_2 NS + e_3 RS + \dots \\ \dots + e_4(\mathbf{M} - \mathbf{M}_h) + e_5(\mathbf{M} - \mathbf{M}_h)^2 & \mathbf{M} \leq \mathbf{M}_h \\ e_0 U + e_1 SS + e_2 NS + e_3 RS + \dots \\ \dots + e_6(\mathbf{M} - \mathbf{M}_h) & \mathbf{M} > \mathbf{M}_h \end{cases} \qquad (2)$$

where U, SS, NS, and RS are dummy variables, with a value of 1 for unspecified, strike-slip, normal-slip, and reverse-slip fault types, respectively, and 0 otherwise; the hinge magnitude $\mathbf{M}_h$ is period dependent, and e_0, e_1, e_2, e_3, e_4, e_5, and e_6 are model coefficients.

The path function is given by:

$$F_P(R_{JB}, \mathbf{M}) = [c_1 + c_2(\mathbf{M} - \mathbf{M}_{ref})] \ln(R/R_{ref}) + (c_3 + \Delta c_3) \times (R - R_{ref}) \tag{3}$$

where:

$$R = \sqrt{R_{JB}^2 + h^2} \tag{4}$$

and c_1, c_2, c_3, Δc_3, $\mathbf{M}_{ref}$, R_{ref}, and h are model coefficients. Parameter Δc_3 is region-dependent.

The site function is given by:

$$F_S(V_{S30}, \mathbf{M}, mech, R_{JB}) = \ln(F_{lin}) + \ln(F_{nl}) \tag{5}$$

where F_{lin} represents the linear component of site amplification and F_{nl} represents the non-linear component of site amplification.

The linear component of the site model (F_{lin}) describes the scaling of ground motion with V_{S30} for linear soil response conditions (i.e., small strains) as follows:

$$\ln(F_{lin}) = \begin{cases} c \ln\left(\frac{V_{S30}}{V_{ref}}\right) & V_{S30} \le V_c \\ c \ln\left(\frac{V_c}{V_{ref}}\right) & V_{S30} > V_c \end{cases} \tag{6}$$

where V_{ref} represents a reference velocity where the amplification is zero (in ln units), V_c is a limiting velocity beyond which there is no further V_{S30}-scaling, and c represents the level of V_{S30}-scaling for $V_{S30} < V_c$.

The function for the F_{nl} term is as follows:

$$\ln(F_{nl}) = f_1 + f_2 \ln\left(\frac{PGA_r + f_3}{f_3}\right) \tag{7}$$

where f_1, f_2, and f_3 are model coefficients and PGA_r is obtained by evaluating Equation 1 for the given $\mathbf{M}$, *mech*, and R_{JB} with $V_{S30} = 760$ m/s. Parameter f_2 represents the degree of nonlinearity for the vertical-component and is formulated as:

$$f_2 = f_4[\exp\{f_5(\min(V_{s30}, 760) - 360)\} - \exp\{f_5(760 - 360)\}] \tag{8}$$

where f_4 and f_5 are model coefficients.

ALEATORY-UNCERTAINTY FUNCTION

The total standard deviation σ is partitioned into components that represent between-event variability (τ) and within-event variability (ϕ) as follows:

$$\sigma(\mathbf{M}) = \sqrt{\phi^2(\mathbf{M}) + \tau^2(\mathbf{M})} \tag{9}$$

The **M**-dependent between-event standard deviation τ is given by:

$$\tau(\mathbf{M}) = \begin{cases} \tau_1 & \mathbf{M} \leq 4.5 \\ \tau_1 + (\tau_2 - \tau_1)(\mathbf{M} - 4.5) & 4.5 < \mathbf{M} < 5.5 \\ \tau_2 & \mathbf{M} \geq 5.5 \end{cases} \tag{10}$$

The **M**-dependent within-event standard deviation ϕ is given by:

$$\phi(\mathbf{M}) = \begin{cases} \phi_1 & \mathbf{M} \leq 4.5 \\ \phi_1 + (\phi_2 - \phi_1)(\mathbf{M} - 4.5) & 4.5 < \mathbf{M} < 5.5 \\ \phi_2 & \mathbf{M} \geq 5.5 \end{cases} \tag{11}$$

V/H MODEL

Because V/H ratios are commonly used in practice, some users may wish to directly predict this quantity. Bozorgnia and Campbell (2016b) have shown that H and V GMPEs can be combined to produce a model for V/H as follows:

$$\mu_{\ln V/H} = \mu_{\ln V} - \mu_{\ln H} \tag{12}$$

where $\mu_{\ln}$ indicates the log mean; hence, $\mu_{\ln V}$ is the mean model from this paper (i.e., Equation 1 with ε_n set to zero) and $\mu_{\ln H}$ is the corresponding mean model from BSSA14. The corresponding standard deviation is:

$$\sigma_{\ln V/H} = \sqrt{\phi_{\ln V/H}^2 + \tau_{\ln V/H}^2} \tag{13a}$$

$$\phi_{\ln V/H} = \sqrt{\phi_{\ln V}^2 + \phi_{\ln H}^2 - 2\rho_{\ln V, \ln H}^W \phi_{\ln V} \phi_{\ln H}} \tag{13b}$$

$$\tau_{\ln V/H} = \sqrt{\tau_{\ln V}^2 + \tau_{\ln H}^2 - 2\rho_{\ln V, \ln H}^B \tau_{\ln V} \tau_{\ln H}} \tag{13c}$$

where $\sigma_{\ln V}$, $\phi_{\ln V}$, and $\tau_{\ln V}$ are total, within-event, and between-event variability for the vertical component (as in Equations 9–11) and the use of H in the subscript denotes the horizontal counterparts from BSSA14. Variables $\rho_{\ln V, \ln H}^W$ and $\rho_{\ln V, \ln H}^B$ are within- and between-event correlation coefficients between the residuals of horizontal and vertical GMPEs (given by Bozorgnia and Campbell 2016b).

DEVELOPMENT AND INTERPRETATION OF REGRESSION RESULTS

As with BSSA14, we developed our GMPEs in three phases. Phase 1 was used to preset coefficients in the site amplification model and the anelastic attenuation coefficient c_3, which would not be well-constrained if left as free parameters in the regression. Phase 2 comprised the main regression for the event and path terms in the base-case model. Phase 3 consisted of mixed-effects regression analyses to check model performance and derive the standard deviation model. Some of the preset parameters from Phase 1 were adjusted on the basis of Phase 3 analyses, as described in the sections below.

PHASE 1: PRESETTING SITE AND ANELASTIC ATTENUATION PARAMETERS

Site Parameters

The initial values of site parameters were developed by SSBA13 through a process of residuals analysis of vertical data relative to the BSSA14 (horizontal-component) model. A subset of the data was used, generally having $R_{JB} < 80$ km in order to minimize the effects of misfit in anelastic attenuation. The considered subset of data had 8,075 recordings for PGA. Using that data, we computed residuals as follows:

$$R_{ij} = \ln Y_{ij} - \mu_{ij}(\mathbf{M}, mech, R_{JB}, V_{S30}) \tag{14}$$

Index i refers to the earthquake event, and index j refers to the recording within event i. Term Y_{ij} represents the observed vertical-component ground motion, and $\mu_{ij}(\mathbf{M}, mech, R_{JB}, V_{S30})$ represents the horizontal-component GMPE mean in natural log units. We then partitioned the residuals using mixed effects analysis (Pinheiro et al. 2013) as follows:

$$R_{ij} = c_k + \eta_i + \varepsilon_{ij} \tag{15}$$

where c_k is the mean residual, η_i is an event term, and ε_{ij} is the within-event residual. An iterative process was employed by SSBA13 to develop preliminary vertical GMPEs. In that process, a series of mixed-effects analyses were performed to investigate site terms, as well as various source and path terms. Within each iteration, model coefficients were adjusted to remove trends. Ultimately, the site, focal mechanism, and distance attenuation terms were thereby modified relative to those for the horizontal component. Only the site and anelastic coefficients from SSBA13 were carried forward as preset parameters in the present model.

The V_{S30}-scaling coefficients (c) that resulted from the SSBA13 analyses are shown in Figure 3 (gray circles); note that in SSBA13 the coefficients were developed only to a maximum period of 3 s. The c values for the vertical-component are significantly lower than those for horizontal, indicating a relatively weak site effect. Similar differences in horizontal and vertical site amplification have been observed previously by Gülerce and Abrahamson (2011) for periods $T < 1.5$ s (i.e., their a_{10} term) and Bommer et al. (2011) over the period range of 0–3 s (i.e., their b_7 and b_8 parameters). Interestingly, Gülerce and Abrahamson (2011) observed stronger vertical than horizontal site response for $T \geq 2$ s, which we did not find. The lesser amplification for the vertical-component observed here is consistent with the widely used technique of taking H/V as a rough measure of site response, under the assumption that vertical-component amplification is negligible in comparison to that of the horizontal (e.g., Lermo and Chavez-Garcia 1993, Ghofrani et al. 2013). The final c values shown in Figure 3 (labeled as "this study") were adjusted at long periods based on Phase 3 residuals analyses discussed further below.

SSBA13 found a small (but significantly non-zero) nonlinearity component in the vertical data, from which parameter f_4 was set as shown in Figure 4. Parameter f_5 was unchanged from BSSA14. In Equation 8, nonlinearity in site amplification (f_2) is directly proportional to f_4, so the much smaller values of f_4 for the vertical component relative to the horizontal (BSSA14) indicate a much lesser degree of nonlinearity. Nonlinearity in vertical
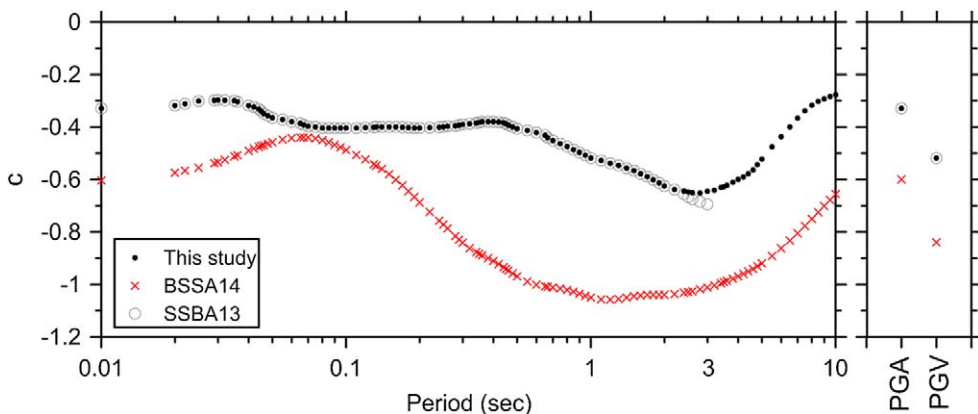
Figure 3. V_{S30}-scaling coefficient c for vertical-component (this study) and horizontal-component (BSSA14) GMPEs. Values marked as SSBA13 were preset initially and subsequently adjusted. The graph to the right shows the results for PGA and PGV (which could not be plotted in the main graph because of the log scale used for period).
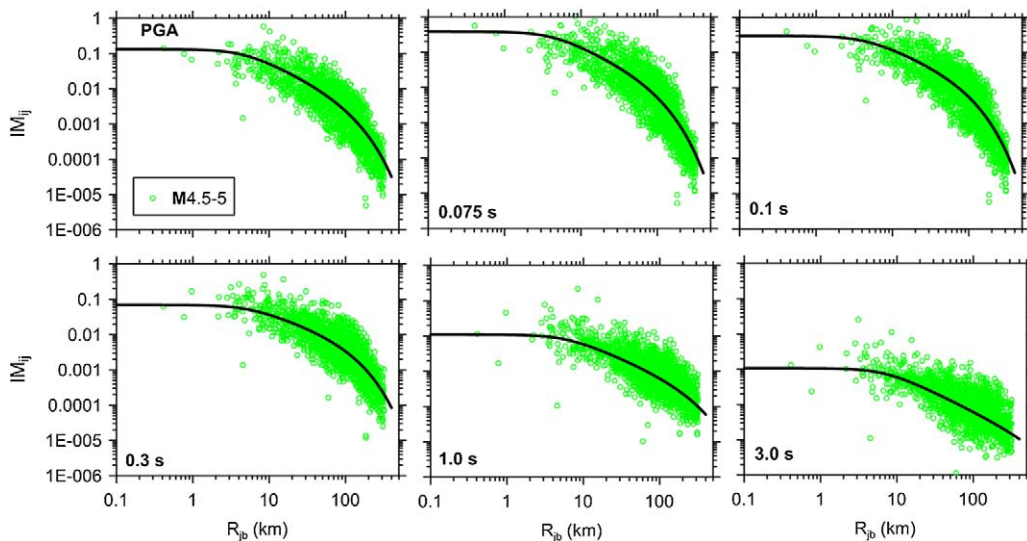
site amplification has not been documented in prior work—we verify this feature of the data using Phase 3 residuals analysis described below and in the online Appendix.

Apparent Anelastic Attenuation Parameter, c_3

We developed preliminary estimates of c_3 following the procedure of BSSA14 (see also SSBA13), using California data for events of $\mathbf{M} < 5.5$. After applying a site correction

Figure 4. Site nonlinearity coefficient f_4 for vertical-component (this study) and horizontal-component (BSSA14) GMPEs. Coefficient f_5 is unchanged from BSSA14 and is not shown. The graph to the right shows the results for PGA and PGV (which could not be plotted in the main graph because of the log scale used for period).

Figure 5. California vertical data and fitted curve (Equation 16) for **M** 4.5–5.0 events. Data corrected to $V_{S30} = 760 \, \text{m/s}$.

to adjust the data to an equivalent V_{S30} of $760 \, \text{m/s}$, the IMs were plotted against distance (as shown, e.g., in Figure 5), and an expression with the following form was fit to the data:

$$\ln Y_{ij} = \eta_i' + c_1' \ln(R/R_{ref}) + c_3(R - R_{ref}) \tag{16}$$

In this expression, c_1' represents apparent geometric spreading within the **M** bin, and c_3 represents the apparent anelastic attenuation. Figure 5 shows strong effects of apparent anelastic attenuation at high frequencies by the curvature of the attenuation with distance. No curvature is observed for $T \geq 1 \, \text{s}$, indicating a lack of significant anelastic attenuation effects.

As with BSSA14 for the horizontal component, when regression results are compiled across the various **M** bins, c_3 is found to be effectively independent of **M**. Figure 6 shows the c_3 values derived from this process relative to those for the horizontal component (from BSSA14). We note that the vertical anelastic attenuation is stronger than the horizontal, which is likely due to vertical-component PSA being controlled by higher-frequency components of the ground motion than for horizontal. A similar observation was made by Bindi et al. (2011); however, they also found anelastic attenuation effects even at long periods (up to 2 s), which we did not. Gülerce and Abrahamson (2011) and Bommer et al. (2011) did not include an anelastic attenuation parameter in their GMPEs.

We adopted average values of c_3 from SSBA13 as preset parameters for the vertical GMPEs. The final c_3 values ("this study") shown in Figure 6 are adjusted based on Phase 3 residuals analyses, discussed further below, along with Δc_3 adjustments for regions outside of California.
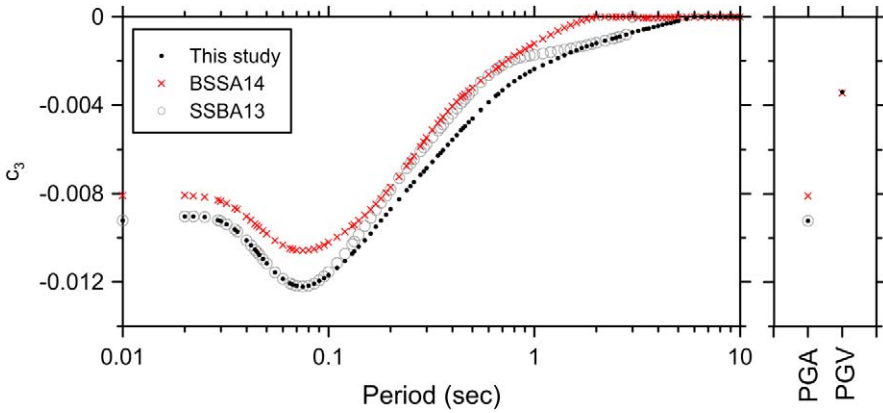
Figure 6. Apparent anelastic attenuation coefficient c_3 based on small **M** data from California using vertical-component data (this study) and horizontal-component data (BSSA14). Values marked as SSBA13 were preset initially in this study and subsequently adjusted. The graph to the right shows the results for PGA and PGV (which could not be plotted in the main graph because of the log scale used for period).

PHASE 2: BASE-CASE REGRESSIONS

Prior to the Phase 2 regressions, all selected IMs were adjusted to the reference velocity of 760 m/s, using the site amplification model discussed earlier. The coefficients for the F_P and F_E terms in Equation 1 were derived in Phase 2 analyses, with the exception of the coefficients c_3 (derived in Phase 1) and Δc_3 (derived in Phase 3). As in BSSA14, the Phase 2 regressions follow the two-stage regression procedure described by Joyner and Boore (1993, 1994), using main shock (CL1) data from events with at least four recordings within 80 km (only those records within 80 km are used); this data subset has 7,001 records. The two stages of the regression are described in the following.

Stage 1 Analysis for Path Term

In Stage 1, path coefficients are evaluated by regressing observations $\ln Y_{ij}$ against the following base-case path relationship $F_{P,B}$ (the base-case excludes Δc_3):

$$F_{P,B}(R_{JB}, \mathbf{M}) = (\overline{\ln Y})_i + [c_1 + c_2(\mathbf{M} - \mathbf{M}_{ref})]\ln(R/R_{ref}) + c_3(R - R_{ref}) \qquad (17)$$

where $(\overline{\ln Y})_i$ represents average observations for event i adjusted to $R = R_{ref}$. As explained further in Boore et al. (2013), we set $R_{ref} = 1$ km and $\mathbf{M}_{ref} = 4.5$. With c_3 constrained, these regressions establish c_1, c_2, and h, as well as $(\overline{\ln Y})_i$ for each earthquake. Parameters c_1 and c_2 describe geometric spreading, with c_2 capturing its **M**-dependence.

Stage 2 Analysis for Source Term

In Stage 2, the $(\overline{\ln Y})_i$ terms from Stage 1 (subsequently referred to as $\overline{\ln Y}$) were used in weighted regressions against **M** to evaluate source terms e_0 to e_6, which control **M**-scaling and source-type effects. Figure 7 shows representative plots of $\overline{\ln Y}$ vs **M**, along with
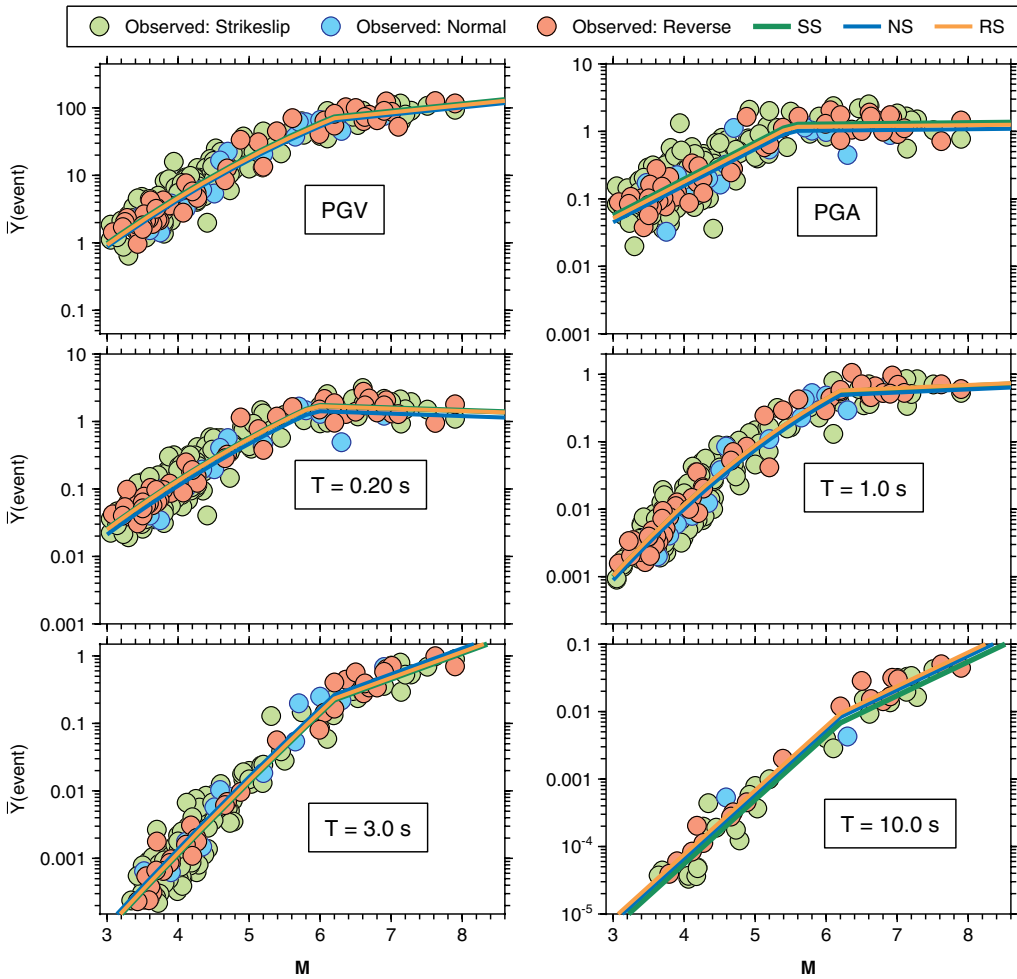
Figure 7. $\bar{Y}$ data points for each event (describing average amplitude at near distances) and fitted **M**-scaling function. All frames span four orders of magnitude in $\bar{Y}$.

regression fits developed as described below. There is a clear change in the slope of the magnitude dependence over a relatively small span of magnitude, which we refer to as the hinge magnitude ($\mathbf{M}_h$). For $\mathbf{M} > \mathbf{M}_h$, slopes are relatively flat for short-period IMs, but steepen as period increases.

The source term function (Equation 2), which was arrived at after many trials, consists of two polynomials hinged at $\mathbf{M}_h$; a quadratic for $\mathbf{M} < \mathbf{M}_h$ and a linear function for $\mathbf{M} > \mathbf{M}_h$. We found that for some periods the quadratic function had a slight upward curvature when plotted vs. **M**. The curvature was very small, but for aesthetic reasons we redid the regression in such cases, with a linear function replacing the quadratic function. As discussed in Boore et al. (2014), there was no constraint on the sign of the slope of the linear function for $\mathbf{M} > \mathbf{M}_h$. We used the values of hinge magnitude $\mathbf{M}_h$ from BSSA14; as shown in Figure 7,

this adequately captures the data trends. Because the source term is a critical part of our GMPEs, we sought to further validate the selected function by plotting the available ground motion data for narrow ranges of R_{JB} as a function of **M**. The *Data Support for **M** Scaling Function* section of the online appendix presents these plots, which support the selected function.

The fault type coefficients in the Stage 2 regression were computed simultaneously with the **M**-dependence. The coefficients for unspecified fault type (e_0) were then computed as a weighted average of the SS, NS, and RS coefficients (e_1, e_2, and e_3); the weights are given in Boore et al. (2013).

Smoothing of Coefficients

Coefficients were obtained separately for each period using the two-stage regression analysis. We then undertook a smoothing process in which we first smoothed the h parameter, re-regressed the model using those values, then computed 11-point running means of the resulting coefficients (and 9-, 7-, 5-, and 3-point operators near the ends of the period range). As the smoothing operator did not affect the coefficients at the last period for which regressions were performed ($T = 10\,\text{s}$), we manually replaced the values at a few periods to ensure smoothness.

PHASE 3: MIXED EFFECTS RESIDUALS ANALYSIS

Phase 3 is comprised of mixed effects residuals analyses having the following purposes: (1) to check the **M**-, R_{JB}-, and V_{S30}-scaling of base-case GMPEs from Phase 1 and 2 analyses and to adjust model parameters as needed to remove trends; (2) to check for possible regional trends of residuals against R_{JB} and V_{S30}; and (3) to check for trends against additional source-related variables not including in the GMPEs (rupture depth, fault tip, rake angle). We used the data selection criteria given in the *Data Sources* section above, which differ from those used in Phase 2 in that we include CL2 events (aftershocks) and data with $R_{JB} > 80\,\text{km}$. Aftershocks are included because we have previously found for the horizontal component of ground motion that between-event residuals for CL1 events are not significantly different from their "child" CL2 events (Boore et al. 2014); hence we consider CL2 data suitable for checking scaling relationships.

Residuals R_{ij} were taken as the log difference between observed amplitudes and GMPE means as given in Equation 14, with the mean model now being the base-case vertical GMPEs from Phases 1 and 2. Residuals were then partitioned into mean misfit (c_k), between-event components (η_i), and within-event components (ε_{ij}), as given in Equation 15. Residuals trends evaluated from the between- and within-event components led to several model adjustments and refinements. We describe this process below, followed by a discussion of the mean bias c_k for the final model.

M-, R_{JB}, and Site-Scaling Evaluated Using Full Data Set

The robustness of the source term is evaluated in Figure 8 by plotting between-event residuals η_i against **M**. The residuals and their binned medians generally have a flat trend with **M**, indicating satisfactory **M**-scaling in the model. (Note: The results shown in Figure 8 are for the final GMPE, with several adjustments as discussed in the following,
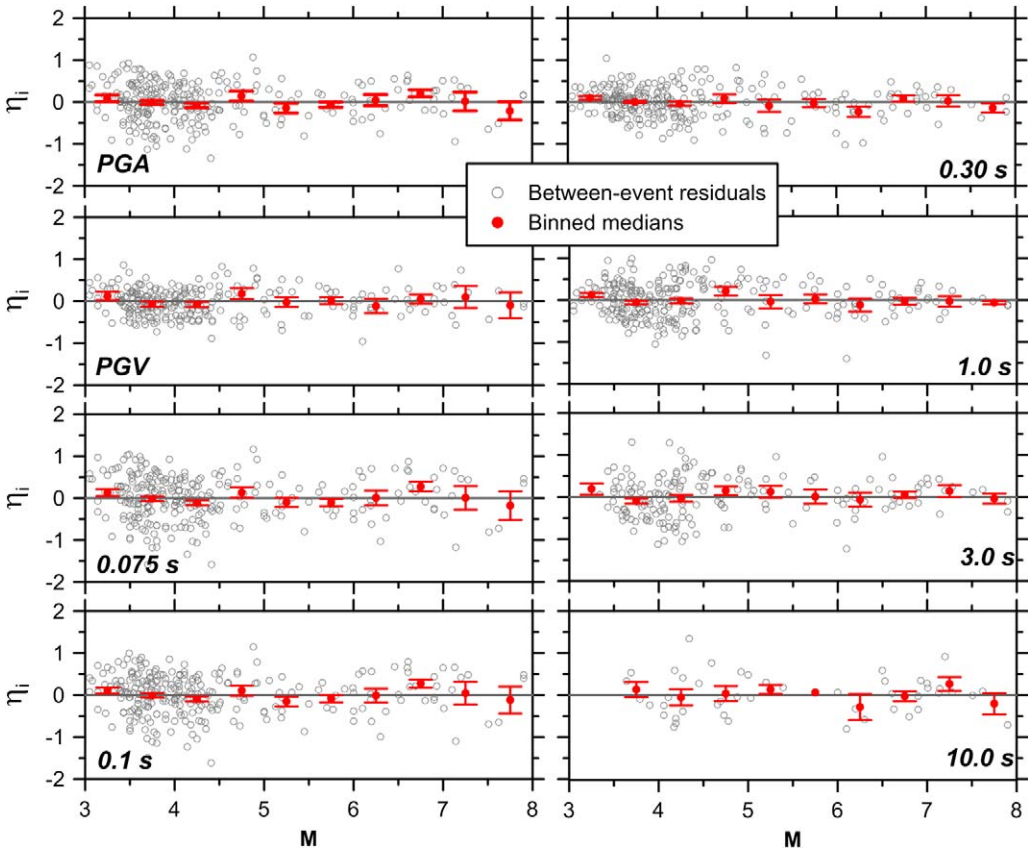
Figure 8. Variations of between-event residuals with **M**. Medians within distance bins are shown along with their 95% confidence intervals.

but those adjustments did not appreciably affect source scaling, which was stable as refinements to the path and site models were made.) We acknowledge some local fluctuations in the residuals (e.g., positive bias, indicating under-prediction, between **M** 6.5–7.0 at short periods). Such features are practically unavoidable for any smooth **M**-scaling function and are modified, but not removed, through alternative values of $\mathbf{M}_h$.

The path term is evaluated by plotting within-event residuals ε_{ij} against R_{JB} for the full (global) Phase 3 data set, as shown in Figure 9. When plots of this type were made using the initial base case model, using the preset parameters for c_3 from SSBA13 (shown in Figure 6), the residuals were found to have an upward trend for PSAs within the period range of 0.1 to 1.0 s, for distances beyond several hundred km. Accordingly, c_3 was adjusted downward as shown in Figure 6 (to the values marked "this study"). With these adjustments, residuals trends were flattened for $R_{JB} < 300$ km, to produce the results shown in Figure 9. Positive bias is encountered for high-frequency ground motions for $R_{JB} > 300$ km, and we do not consider the model to be applicable at these large distances. It is possible that this positive
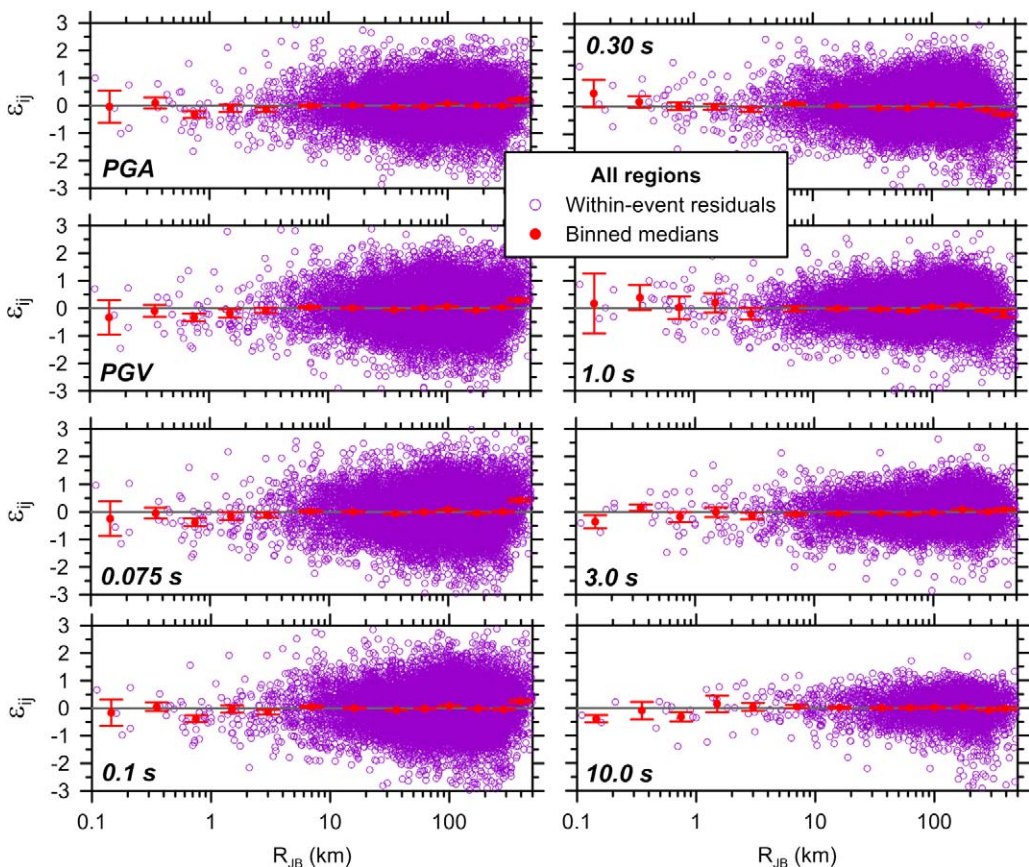
Figure 9. Variations of within-event residuals with R_{JB} for final model, after c_3 adjustment (shown in Figure 6). Medians within distance bins are shown along with their 95% confidence intervals.

bias is influence by data selection criteria from BSSA14 that are not optimized for the vertical component of ground motion.

A similar process to that employed to analyze the path residuals was undertaken for the site term. Using the global Phase 3 data set, we found the V_{S30}-scaling using preset values of scaling parameter c to be slightly too-fast for periods near the upper end of the range considered by SSBA13 (near $T = 3.0\,\text{s}$). This observation, combined with the need to extend the model to $T = 10\,\text{s}$, led with some iteration to the c values marked in Figure 3 as "this study." No changes to the original SSBA13 values were applied for $T \leq 2.0\,\text{s}$. Figure 10 shows the trends of ε_{ij} against V_{S30} following this adjustment. We note that the trends are flat with respect to V_{S30} except for: (1) negative residuals for $V_{S30} < 200$ m/s and mid- to long-period IMs (PGV and PSA for $T > 1$ s) and (2) negative residuals for $V_{S30} > 600$ m/s and short-period IMs (PGA and PSA for $T < 0.7$ s). Removing these trends from the data would require multi-segment V_{S30}-scaling functions that we consider too complex for the present GMPEs.
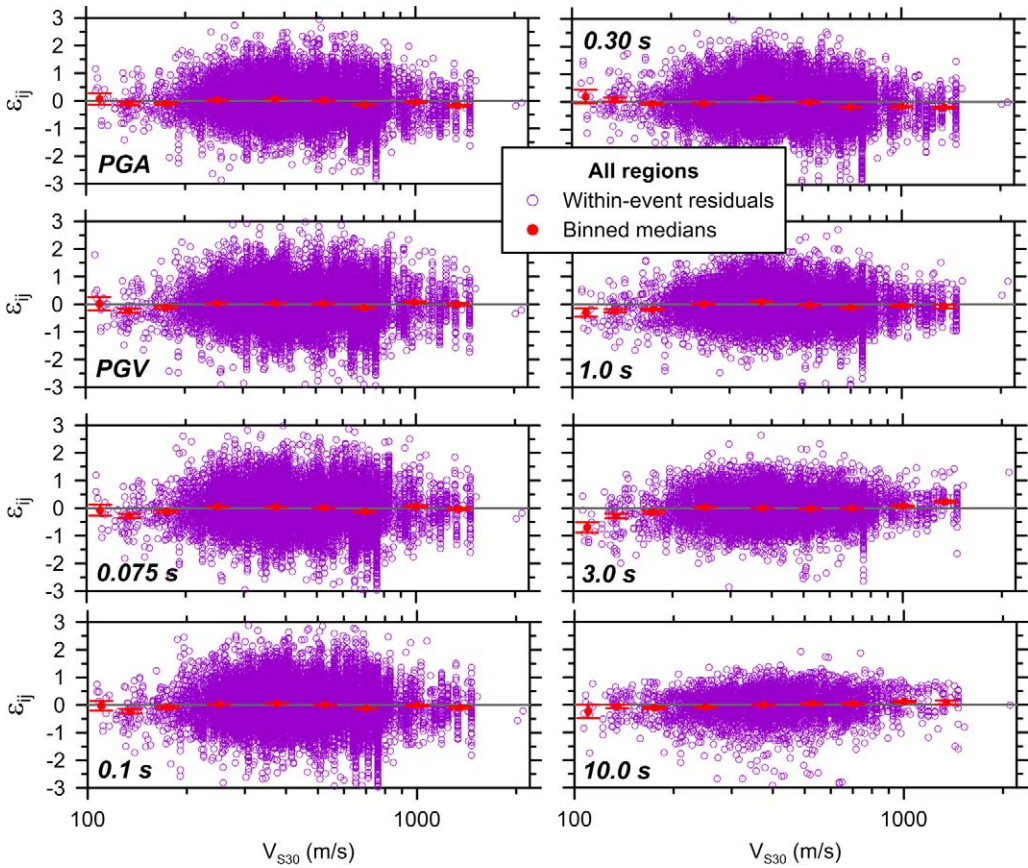
Figure 10. Variations of within-event residuals with V_{S30} for final model with c adjusted and extended relative to SSBA13. Stars indicate periods where c was changed or extended relative to preset values. Medians within distance bins are shown along with their 95% confidence intervals.

Nonlinearity in the site amplification was checked with additional residuals analyses as described in the *Nonlinear Site Response* section of the online appendix. These analyses support previous findings (SSBA13) that the vertical NGA-West2 ground motions exhibit smaller levels of nonlinearity than for the horizontal component motions. These additional analyses did not lead to any changes to the nonlinear site parameter f_4 relative to those shown in Figure 4.

Regional Effects

Because we found regional variations in the anelastic attenuation coefficient for horizontal ground motions, the BSSA14 model included a correction term Δc_3 that was applied to some regions outside of California. For vertical-component ground motions, we plot within-event residuals against R_{JB} by region in Figure 11. The need for a Δc_3 term is indicated by a curved trend in the residuals for distances beyond about 70 km. As expected, the California
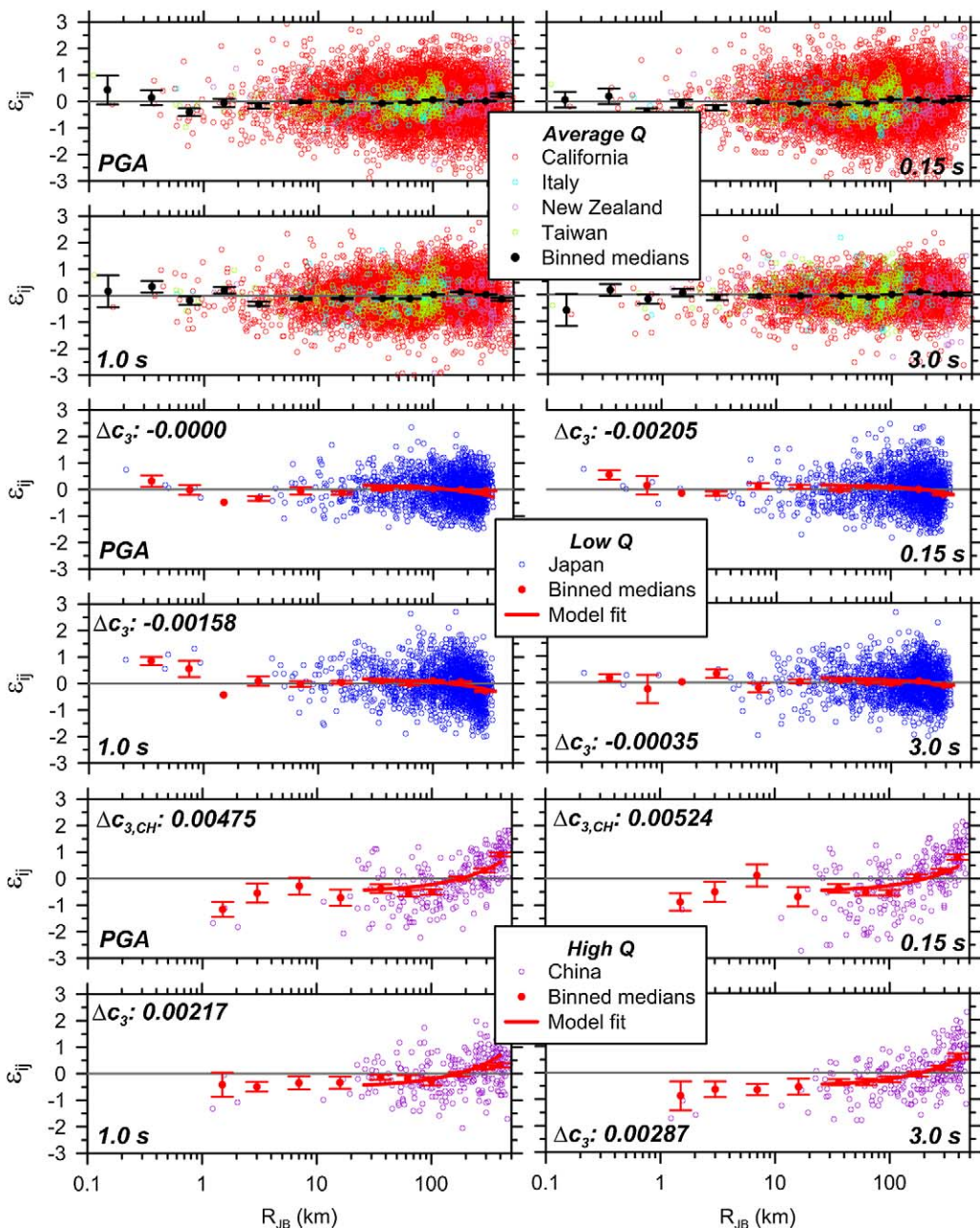
Figure 11. Within-event residuals for regions identified as average, low, or high Q. Also shown is the fit line per Equation 16 for $R_{JB} > 25–50$ km. Medians within distance bins are shown along with their 95% confidence intervals.

data have a flat trend ($\Delta c_3 = 0$) and are indicated as having "average Q" in Figure 11 (where Q is the crustal quality factor widely used in seismology). The data from Italy, New Zealand, and Taiwan also have flat trends; in the case of Italy, this result is different from the horizontal-component, which decayed more rapidly than for the global data set (we say that this is a low-Q trend, because a low Q would give a more rapid attenuation). As with the horizontal-component motions, downward trends are found for Japan (low Q) and upward trends for China (high Q). Data from Turkey had mixed trends for different period ranges (high Q for $T < 0.15$ s; average Q otherwise) and are not included in Figure 11. We caution that country names are used as a convenient short-hand to describe the regions, realizing that results for the region may well be applicable beyond the political boundaries of the country and that regional differences of attenuation may occur within the countries; at this time, we do not have sufficient data to establish the geographic limits of our results nor to parse the data more finely.

For the low and high Q cases, we fit a linear expression through the data according to:

$$\varepsilon = \Delta c_3 (R - R_{ref}) + \bar{\varepsilon}_{lR} \tag{18}$$

where Δc_3 is the additive regional adjustment to the c_3 term from Equation 3, and $\bar{\varepsilon}_{lR}$ is the mean value of the residuals at close distance in a given region. In order to prevent the relatively-sparse data at the closest distances from affecting the slope Δc_3, we limited the data range used in the regression to $R_{JB} > 25-50$ km (the lower distance limit was adjusted within this range depending on the characteristics of the data and varies by region and period). This captures the "flat" portion of the residuals at relatively close distances before anelastic effects become significant (beyond about 80 km). Fits according to Equation 18 are included in Figure 11. Values of Δc_3 are given in the figure for the low and high Q cases and are compiled as regression coefficients. These regional adjustments were included in the computation of residuals elsewhere in this manuscript.

For comparison, Bozorgnia and Campbell (2016a), Chiou and Youngs (2013), and Gülerce et al. (2016) have anelastic corrections akin to low Q for Italy and Japan and high Q for China. Gülerce et al. (2016) also show high Q for the Middle East region.

Regional trends in V_{S30}-scaling were investigated in a similar manner by plotting within-event residuals against V_{S30} by region. The results are presented in the *Regional Site Response* section of the online appendix and generally show no appreciable regional variations. Other NGA-West2 GMPEs include a regional adjustment to V_{S30}-scaling for Japan and Taiwan (Chiou and Youngs 2013); Japan-only (Bozorgnia and Campbell 2016a); and Japan, Italy, and Taiwan (Gülerce et al. 2016).

Effects of Source Parameters Not Included in GMPEs

During GMPE development, we investigated possible effects of several parameters that were ultimately not selected for inclusion in the model. These parameters include depth to top of rupture (Z_{tor}), depth to hypocenter (Z_{hypo}), and fault dip (δ). Plots of event terms against these parameters are included in the *Residual Trends against Source Variables Not Included in GMPEs* section of the online appendix. The results indicate

no trends that we consider sufficiently important to justify including the respective parameters in the GMPEs.

Mean of Residuals, c_k

As shown in Figure 12, model bias, as represented by the mean residuals c_k, is very small (i.e., $|c_k| < 0.05$) for the base-case GMPE when the Phase 2 data set is used in residuals analysis, as expected. Note that the base-case GMPE used in these calculations reflects the updates to c_3 and c described in prior sections, but does not include Δc_3 corrections, which are relatively unimportant due to data truncation at 80 km. When the larger Phase 3 data set is used (this time with the final GMPEs, including Δc_3 corrections), c_k values increase, reaching peak values of 0.09 at about 1.5 s. The Phase 3 results shown in Figure 12 are based on a maximum R_{JB} distance of 300 km, because this is the recommended limit of model applicability.

The differences between the Phase 2 and Phase 3 data criteria include the 80 km distance cutoff and the omission of CL2 events for Phase 2. Figure 12 shows that the increase is not caused by the use of CL2 data in Phase 3, as c_k values for all Phase 3 data and the subset of Phase 3 data from CL1 events are similar. Instead, the increase is caused by the introduction of data within the distance range $R_{JB} = 80-300$ km. Nonetheless, even with the increase from Phase 3 analysis, the model bias remains sufficiently small that we consider the GMPEs to be suitable for the range of conditions that were considered ($R_{JB} < 300$ km and both CL1 and CL2 events).

ALEATORY UNCERTAINTY MODEL

The aleatory uncertainty model (Equations 9–11) is derived from the Phase 3 residuals analysis and thus represents a relatively large database spanning a broader range of **M** and R_{JB} than was used in Phase 2. The residuals analyses were performed using the mean model given in Equations 1–8, including the regional anelastic attenuation terms.
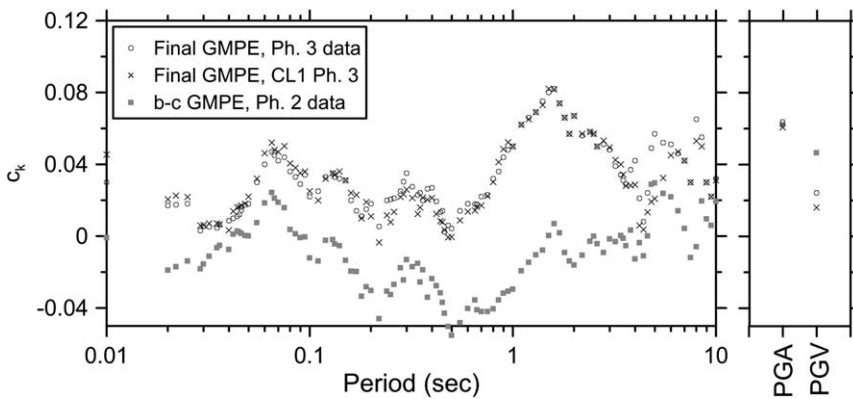

Figure 12. Period-dependence of mean bias c_k for updated base-case (b–c) GMPE with Phase 2 and Phase 3 data sets and final GMPE with full Phase 3 data set and CL1-only subset. Only data with $R_{JB} < 300$ km was used for Phase 3.
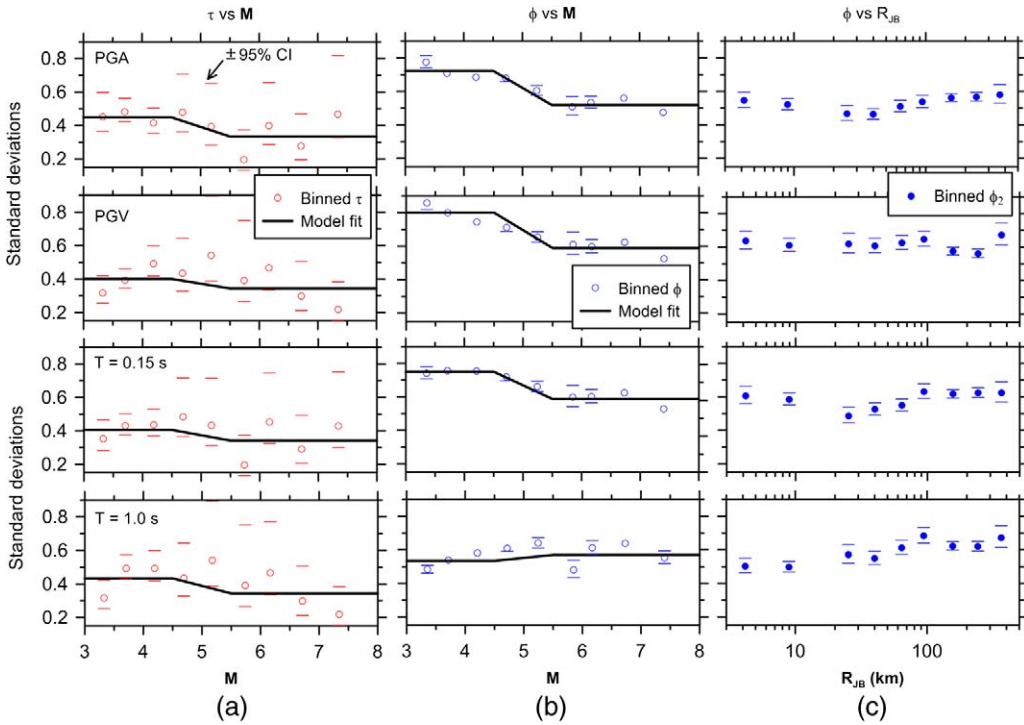
Figure 13. Binned standard deviation terms and 95% confidence intervals. (a) τ against **M**; (b) ϕ against **M**; and (c) ϕ against R_{JB} for **M** > 5.5. Lines in the figures represent model fits per Equations 10 and 11.

As shown in Figure 13a–b, we binned event terms η_i and within-event residuals ε_{ij} by **M** to evaluate the magnitude dependence of between-event standard deviations τ and within-event standard deviations ϕ. We find that τ generally decreases with **M**, whereas ϕ decreases with **M** for $T < 0.85$ s and increases at longer periods. As shown in Figure 13c, we also investigated the distance-dependence of ϕ using within-event residuals for **M** > 5.5. When investigated over many periods, there are some instances where ϕ increases modestly beyond about 60 km (0.3 and 1.0 s), but the general observation is that the trend is flat. Accordingly, we have not developed an R_{JB}-dependent ϕ model for the vertical-component (this is in contrast to the horizontal-component model of BSSA14).

Standard deviation coefficients τ_1, ϕ_1, τ_2, and ϕ_2 were computed using Phase 3 data with $R_{JB} \leq 300$ km. Coefficients τ_1, ϕ_1 are based on all such residuals (η or ε) for **M** < 4.5, whereas τ_2 and ϕ_2 are based on all such residuals with **M** > 5.5. Figure 14 shows the period dependence of the standard deviation terms for **M** > 5.5, with the corresponding terms for the horizontal model shown for comparison. We find τ values are higher for vertical than for horizontal motions, whereas ϕ values are comparable. Because of the increased τ, the overall standard deviation (σ) is higher for the vertical component. The local high in the τ and σ terms
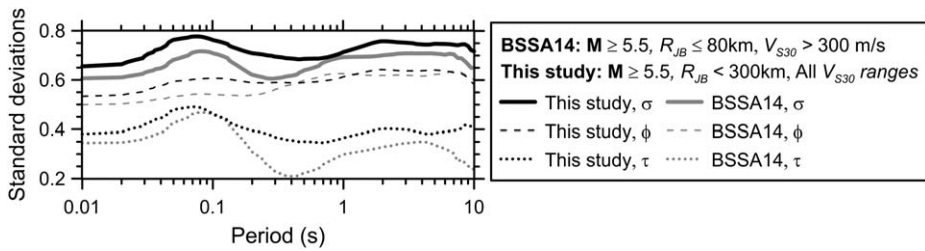
Figure 14. Comparison of vertical- and horizontal-component standard deviation terms from present study and BSSA14 for $\mathbf{M} > 5.5$. The BSSA14 model depends on distance and V_{S30}, which are effects not required for the vertical model. Horizontal results are shown for $R_{JB} < 80$ km and $V_{S30} > 300$ m/s.

near 0.1 s is thought to be a site effect; it is present also for the horizontal-component GMPEs and is discussed further in BSSA14.

VERTICAL GMPE PERFORMANCE

The recommended GMPEs, as given by Equations 1–11, are comprised of similar functions to the horizontal-component GMPEs of BSSA14 but are fully reworked in the Phase 1 to 3 analyses, as described in the previous sections. The model coefficients are given in Table A1 in the online appendix.

Attributes of the GMPEs' median predictions of distance and $\mathbf{M}$ scaling are shown in Figure 15 (we use the term "median" here because the arithmetic median equals the exponent of the natural log mean). The $\mathbf{M}$-scaling, which can be evaluated by the relative positions of the curves in Figure 15 for a given distance, is relatively weak for high-frequency IMs at close distance and is strong at all distances for low frequencies. These features are similar for the vertical and horizontal-components. Likewise, the distance-scaling trends are similar, with both components having $\mathbf{M}$-dependent geometric spreading and anelastic attenuation affects for high frequency IMs for $R_{JB} > \sim 80$ km. Despite the broad similarities, the rate of geometric spreading for vertical motions is somewhat slower than for horizontal motions, especially for $T > 1.0$ s, while the anelastic attenuation is faster for $T = 0.1 - 1.0$ s. The smaller short-distance ground motion amplitudes for most vertical IMs, as compared to horizontal, result in part from higher fictitious depth terms. Other terms account for the relatively large near-fault vertical ground motions at short periods.

Figure 16 shows vertical spectra for a range of magnitudes, $R_{JB} = 20$ km, and rock and soft soil site conditions. The spectra peak near 0.08 to 0.10 s; the locations of this peak do not appreciably change with $\mathbf{M}$ or site condition. These features differ from the horizontal ground motions, which peak at longer periods that, in turn, increase systematically with $\mathbf{M}$ and decrease with V_{S30}. Notable features of vertical site response revealed in Figure 16 are that (1) the difference between the soil and rock curves is not significantly $\mathbf{M}$-dependent, indicating the small impact of nonlinearity (the effect would be greater for a closer R_{JB}, but still much smaller than for the horizontal-component) and (2) the offset between
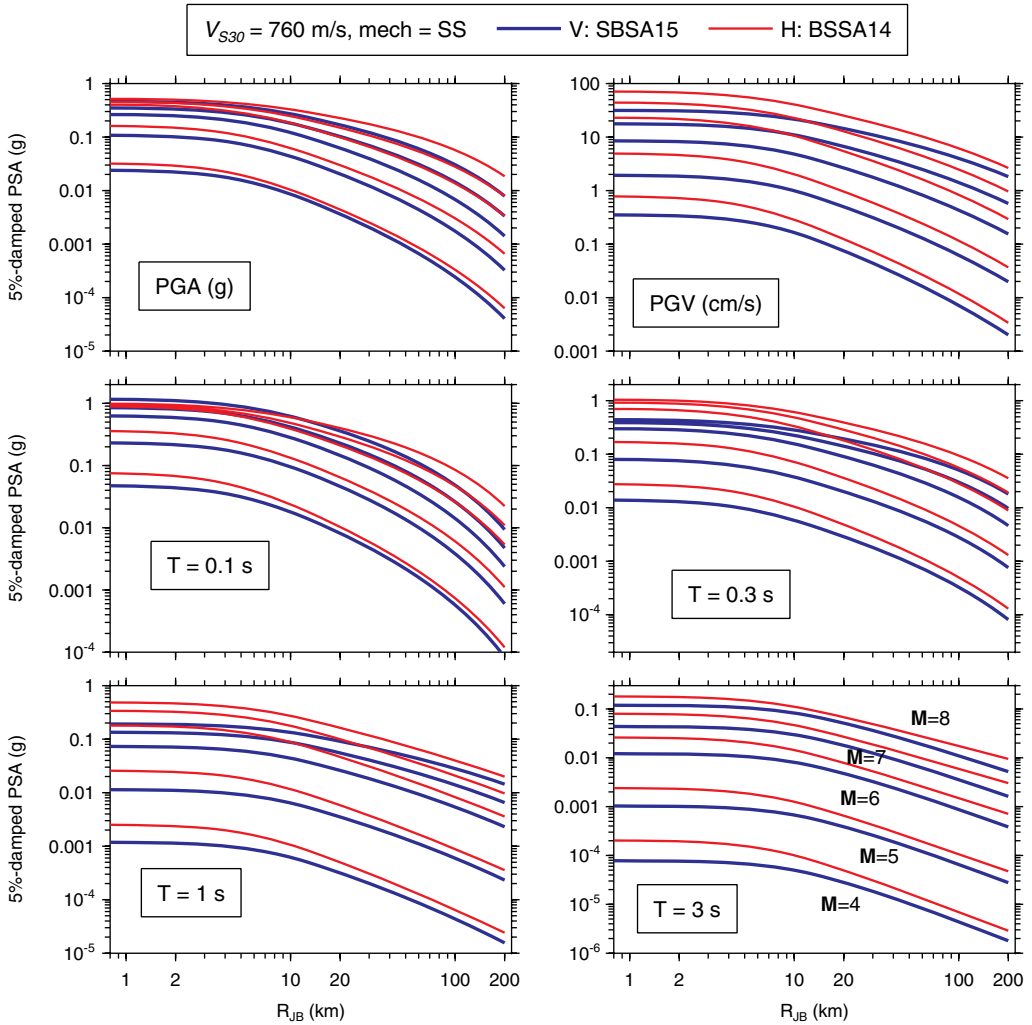
Figure 15. Median trends of proposed vertical GMPEs as compared to horizontal GMPEs from BSSA14, as a function of distance for strike-slip earthquakes and $V_{S30} = 760 \, \text{m/s}$.

rock and soil spectra reaches a local maximum near 3.0 s, but in general is less period-dependent than for the horizontal component.

Figure 17 (left side) shows V/H ratios as a function of period for a range of **M** and $R_{JB} = 10$, 70, and 300 km. V/H is plotted as the ratios of median predictions from the present model and BSSA14 for the site condition of $V_{S30} = 760 \, \text{m/s}$. For $R_{JB} = 10 \, \text{km}$, V/H peaks at values near unity for $T = 0.04$ to 0.06 s then falls off to nearly ½ for $T > {\sim}0.2 \, \text{s}$. Trends of this sort at close distance have been observed previously (e.g., Bozorgnia and Campbell 2004) and were even hypothesized in early work by Richter (1958). As distance increases, V/H becomes relatively flat (at 70 km) and eventually markedly increases with

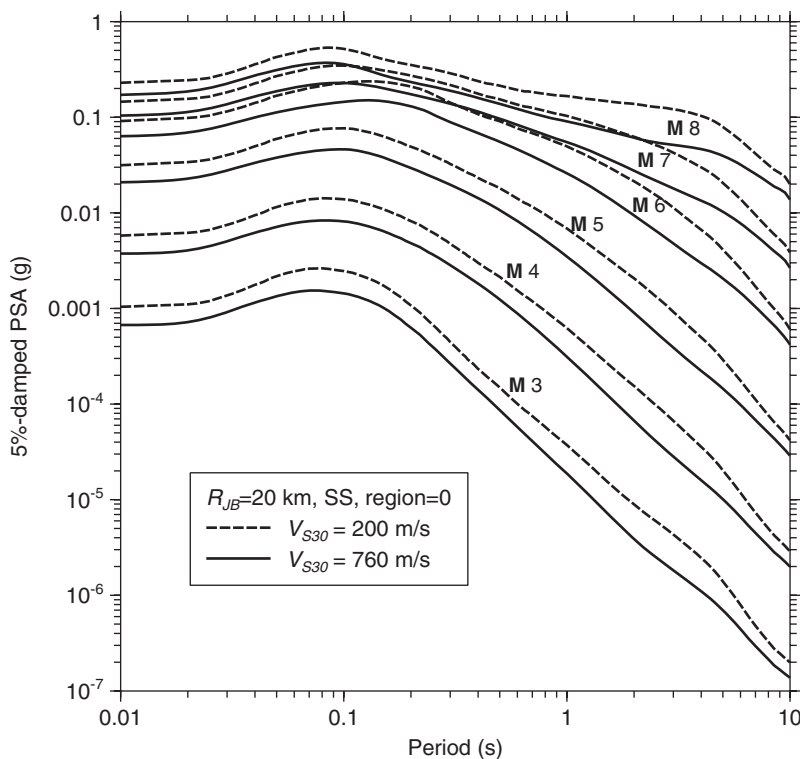**Figure 16.** Median PSA for strike slip earthquakes from proposed vertical GMPEs as function of **M** for $R_{JB} = 20$ km for $V_{S30} = 200$ and 760 m/s.

T (in 300 km plot). The increase of V/H with distance for $T > \sim 0.2$ s is a result of the vertical-component ground motions having slower rates of geometric spreading (which is only partially offset by faster vertical anelastic attenuation). Regional variations in V/H trends at large distances will occur because of the regionally variable Δc_3 parameter. The right side of Figure 17 shows V/H ratios as a function of period for a range of V_{S30} and **M** 7 events at $R_{JB} = 10$, 70, and 300 km. The V_{S30} values used in the plot are medians of NEHRP categories B, C, D, and E (per Seyhan and Stewart, 2014). Because the scaling of the horizontal component is much stronger than that for the vertical, V/H drops for soft soil sites at large distances where nonlinear effects are small. At the closest distance of $R_{JB} = 10$ km, nonlinearity strongly influences the H component at high frequencies for soft sites while exerting a relatively small effect on V; this causes V/H ratios to rise for such conditions (soft soils, close distance, short periods).

SUMMARY AND DISCUSSION

We have presented a set of vertical-component ground motion prediction equations (GMPEs) that we believe are the simplest formulation demanded by the NGA-West2 database. The new relations provide a demonstrably reliable description of vertical recorded ground motion amplitudes for shallow crustal earthquakes in active tectonic regions over
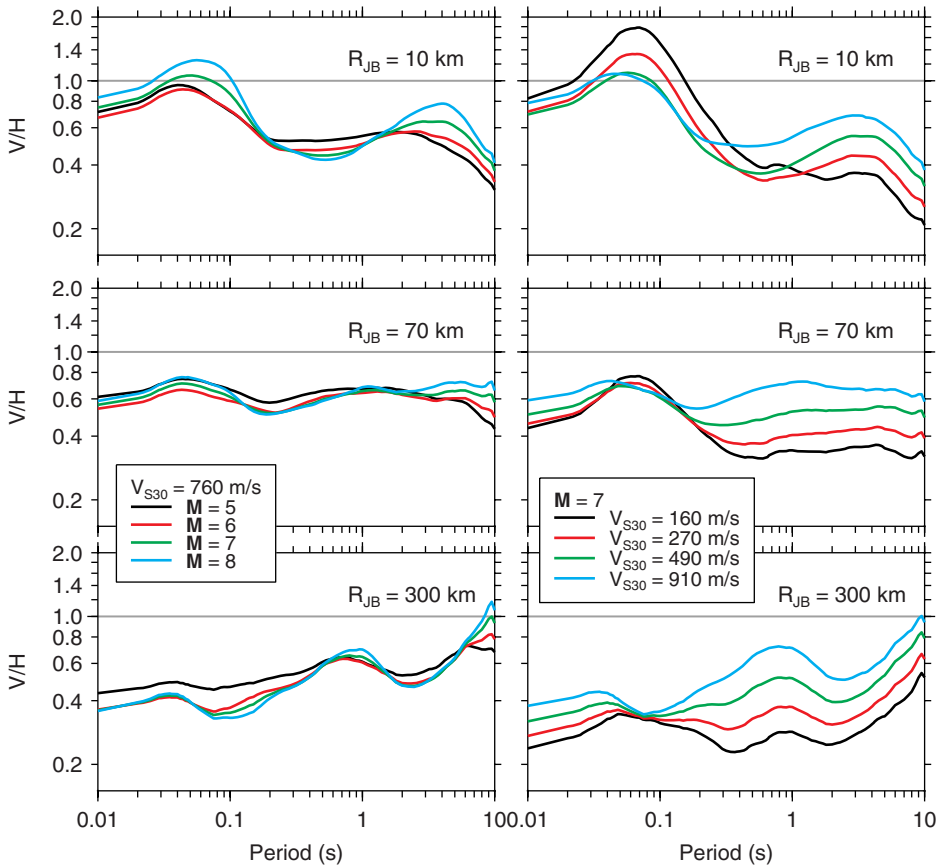
Figure 17. Dependence of V/H spectral ratios on **M** and R_{JB} for $V_{S30} = 760$ m/s (left side) and V_{S30} and R_{JB} for **M** 7 (right side). V/H computed as ratio of median predictions from present study and BSSA14.

a wide range of magnitudes, distances, and site conditions. Our GMPEs are based on: (1) preliminary analyses which are used to preset anelastic attenuation and site coefficients; (2) two-step regressions to determine key scaling parameters; and (3) subsequent model refinements and extensions based on residuals analysis. While the functions for the vertical model are similar to those of BSSA14 for horizontal-component motions, all model components have been reworked, including those for source, path, site, and aleatory uncertainty. Our model coefficients are provided in an online appendix table.

Our GMPEs have some distinguishing characteristics relative to other NGA-West2 models and models from the literature. One such distinguishing feature is our combined polynomial-linear **M**-scaling function, which we support through data analysis both in the form of average ground motions for each event ($\overline{\ln Y}$) and by individual recordings in narrow distance and site condition ranges. This function produces median estimates that are somewhat different from other NGA-West2 models, especially for large **M** events (N. Gregor,

pers. comm., 2015). Another important model feature is the use of a path-scaling function that accounts for **M**-dependent geometric spreading and region-dependent apparent anelastic attenuation. Regional effects are not found in the site function. Our site function is fully empirical and includes V_{S30}-scaling and nonlinear terms. The empirically derived nonlinear site amplification function is a unique feature of our GMPEs.

Our GMPEs are intended for application in tectonically active crustal regions and should not be used for other tectonic regimes unless their applicability can be verified. The data controlling our equations are derived principally from California, Taiwan, Japan, China, the Mediterranean region (Italy, Greece, Turkey), and Alaska. We have demonstrated some regional variations in ground motions, so application of the GMPEs to other areas considered to be active crustal regions carries an additional degree of epistemic uncertainty. This includes regions in the western United States outside of the portions of California included in our data set.

We recommend the following limits for the predictor variables used in our GMPEs:

- Strike-slip and reverse-slip earthquakes, **M** = 3 to 8.0
- Normal-slip earthquakes, **M** = 3 to 7
- Distance, R_{JB} = 0 to 300 km
- Time-averaged shear wave velocities of V_{S30} = 200 to 1,500 m/s (the 200 m/s limit is based on misfits identified from residuals for slower velocities). We note that there is modest over-prediction for $V_{S30} > 600$ m/s for PGA and PSA at $T < 0.7$ s.
- CL1 event types (main shocks). The equations may well be applicable to CL2 events as well, but this has not been demonstrated in the manner undertaken for the horizontal-component by BSSA14.

These limits are subjective estimates based on the distributions of the recordings used to develop the equations and the results of residuals analyses. Our recommended limit of **M**8.0 for strike-slip and reverse-slip earthquakes is near the data limits; the larger limit of **M**8.5 that was used for horizontal-component GMPEs (BSSA14) was supported by simulations that have not been completed for vertical-component ground motions.

ACKNOWLEDGMENTS

APPENDIX

Please refer to the online version of this paper to access the supplementary materials in the online Appendix.

REFERENCES

Akkar, S., Sandıkkaya, M. A., and Ay, B. O., 2014. Compatible ground-motion prediction equations for damping scaling factors and vertical-to-horizontal spectral amplitude ratios for the broader Europe region, *Bull. Earthq. Eng.* **12**, 517–547.

Ancheta, T. D., Darragh, R. B., Stewart, J. P., Seyhan, E., Silva, W. J., Chiou, B. S. J., Wooddell, K. E., Graves, R. W., Kottke, A. R., Boore, D. M., Kishida, T., and Donahue, J. L., 2014. NGA-West2 database, *Earthquake Spectra* **30**, 989–1005.

Ambraseys, N. N., and Douglas, J., 2003. Near field horizontal and vertical earthquake ground motions, *Soil Dyn. Earthq. Eng.* **23**, 1–18.

Ambraseys, N. N., Douglas, J., Smit, P., and Sarma, S. K., 2005. Equations for the estimation of strong ground motions from shallow crustal earthquakes using data from Europe and the Middle East: Vertical peak ground acceleration and spectral acceleration, *Bull. Earthq. Eng.* **3**, 55–73.

Bindi, D., Pacor, F., Luzi, L., Puglia, R., Massa, M., Ameri, G., and Paolucci, R., 2011. Ground motion prediction equations derived from the Italian strong motion database, *Bull. Earthq. Eng.* **9**, 1899–1920.

Bommer, J. J., Akkar, S., and Kale, Ö., 2011. A model for vertical-to-horizontal response spectral ratios for Europe and the Middle East, *Bull. Seism. Soc. Am.* **101**, 1783–1806.

Boore, D. M., Stewart, J. P., Seyhan, E., and Atkinson, G. M., 2013. *NGA-West 2 Equations for Predicting Response Spectral Accelerations for Shallow Crustal Earthquakes*, PEER 2013/05, Pacific Earthquake Engineering Research Center, University of California, Berkeley, 135 pp.

Boore, D. M., Stewart, J. P., Seyhan, E., and Atkinson, G. M., 2014. NGA-West 2 equations for predicting PGA, PGV, and 5%-damped PSA for shallow crustal earthquakes, *Earthquake Spectra* **30**, 1057–1085.

Bozorgnia, Y., and Campbell, K. W., 2004. The vertical-to-horizontal response spectral ratio and tentative procedures for developing simplified V/H and vertical design spectra, *J. Earthq. Eng.* **8**, 175–207.

Bozorgnia, Y., and Campbell, K. W., 2016a. Vertical ground motion model using NGA-West2 database, *Earthquake Spectra* **32**, 979–1004.

Bozorgnia, Y., and Campbell, K. W., 2016b. Vertical-to-horizontal (V/H) ground motion model, *Earthquake Spectra* **32**, 979–1004.

Bozorgnia, Y., Abrahamson, N. A., Al Atik, L., Ancheta, T. D., Atkinson, G. M., Baker, J. W., Baltay, A., Boore, D. M., Campbell, K. W., Chiou, B. S.-J., Darragh, R., Day, S., Donahue, J., Graves, R. W., Gregor, N., Hanks, T., Idriss, I. M., Kamai, R., Kishida, T., Kottke, A., Mahin, S. A., Rezaeian, S., Rowshandel, B., Seyhan, E., Shahi, S., Shantz, T., Silva, W., Spudich, P., Stewart, J. P., Watson-Lamprey, J., Wooddell, K., and Youngs, R., 2014. NGA-West 2 research project, *Earthquake Spectra* **30**, 973–987.

Campbell, K. W., and Bozorgnia, Y., 2003. Updated near-source ground motion (attenuation) relations for the horizontal and vertical components of peak ground acceleration and acceleration response spectra, *Bull. Seismol. Soc. Am.* **93**, 314–331.

Chiou, B. S.-J., and Youngs, R. R., 2013. Ground motion prediction model for vertical component of peak ground motions and response spectra, Chapter 5 in *NGA-West2 Ground Motion*

Prediction Equations for Vertical Ground Motions, PEER Report 2013/24, Pacific Earthquake Engineering Research Center, University of California, Berkeley.

Ghofrani, H., Atkinson, G. M., and Goda, K., 2013. Implications of the 2011 M9.0 Tohoku Japan earthquake for the treatment of site effects in large earthquakes. *Bull. Earthq. Eng.* **11**, 171–203.

Gülerce, Z., and Abrahamson, N. A., 2011. Site-specific design spectra for vertical ground motion, *Earthquake Spectra* **27**, 1023–1047.

Gülerce, Z., Kamai, R., Abrahamson, N. A., and Silva, W. J., 2016. Ground motion prediction equations for the vertical ground motion component based on the NGA-W2 database, *Earthquake Spectra*, in review.

Joyner, W. B., and Boore, D. M., 1993. Methods for regression analysis of strong-motion data, *Bull. Seismol. Soc. Am.* **83**, 469–487.

Joyner, W. B., and Boore, D. M., 1994. Errata: Methods for regression analysis of strong-motion data, *Bull. Seismol. Soc. Am.* **84**, 955–956.

Lermo, J., and Chavez-Garcia, F., 1993. Site effect evaluation using spectral ratios with only one station, *Bull. Seism. Soc. Am.* **83**, 1574–1594.

Pinheiro, H., Bates, D., DebRoy, S., Sarkar, D., and the R Development Core Team, 2013. *NLME: Linear and Nonlinear Mixed Effects Models*, R package version 3.1–108.

Richter, C. F., 1958. Elementary Seismology, W.H. Freeman & Co., San Francisco, CA.

Seyhan, E., and Stewart, J. P., 2014. Semi-empirical nonlinear site amplification from NGA-West 2 data and simulations, *Earthquake Spectra* **30**, 1241–1256.

Stewart, J. P., Seyhan, E., Boore, D. M., and Atkinson, G. M., 2013. SSBA13: Vertical Component Ground Motion Prediction Equations for Active Crustal Regions, Chapter 3 in *NGA-West2 Ground Motion Prediction Equations for Vertical Ground Motions*, PEER Report 2013/24, Pacific Earthquake Engineering Research Center, University of California, Berkeley.

Seyhan, E., Stewart, J. P., Ancheta, T. D., Darragh, R. B., and Graves, R. W., 2014. NGA-West 2 site database, *Earthquake Spectra* **30**, 1007–1024.

Wooddell, K. E., and Abrahamson, N. A., 2014. Classification of main shocks and aftershocks in NGA-West 2, *Earthquake Spectra* **30**, 1257–1267.